On the Maximum Stellar Rotation to form a Black Hole without an Accompanying Luminous Transient

Ariadna Murguia-Berthier[1,2] , Aldo Batta[1,2,3,4] , Agnieszka Janiuk[2,5] , Enrico Ramirez-Ruiz[1,2] , Ilya Mandel[2,6,7,8] , Scott C. Noble[9] , and Rosa Wallace Everson[1,2]

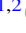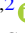[1] Department of Astronomy and Astrophysics, University of California, Santa Cruz, CA 95064, USA
[2] DARK, Niels Bohr Institute, University of Copenhagen, Blegdamsvej 17, DK-2100 Copenhagen, Denmark
[3] Instituto Nacional de Astrofísica, Óptica y Electrónica, Tonantzintla, Puebla 72840, México
[4] Consejo Nacional de Ciencia y Tecnología, Av. Insurgentes Sur 1582, Col. Crédito Constructor, CDMX, C.P. 03940, Mexico
[5] Centrum Fizyki Teoretycznej PAN Al. Lotników 32/46, 02-668 Warsaw, Poland
[6] Monash Centre for Astrophysics, School of Physics and Astronomy, Monash University, Clayton, Victoria 3800, Australia
[7] The ARC Center of Excellence for Gravitational Wave Discovery—OzGrav, Australia
[8] Institute of Gravitational Wave Astronomy and School of Physics and Astronomy, University of Birmingham, Birmingham B15 2TT, UK
[9] Gravitational Astrophysics Laboratory, NASA Goddard Space Flight Center, Greenbelt, MD 20771, USA

Abstract

The collapse of a massive star with low angular momentum content is commonly thought to result in the formation of a black hole without an accompanying bright transient. Our goal in this Letter is to understand the flow in and around a newly formed black hole, involving accretion and rotation, via general relativistic hydrodynamics simulations aimed at studying the conditions under which infalling material can accrete without forming a centrifugally supported structure and, as a result, generate no effective feedback. On the other hand, if the feedback from the black hole is significant, the collapse would be halted and we suggest that the event is likely to be followed by a bright transient. We find that feedback is only efficient if the specific angular momentum of the infalling material at the innermost stable circular orbit exceeds that of geodesic circular flow at that radius by at least $\approx 20\%$. We use the results of our simulations to constrain the maximal stellar rotation rates of the disappearing massive progenitors PHL293B-LBV and N6946-BH1, and to provide an estimate of the overall rate of disappearing massive stars. We find that about a few percent of single O-type stars with measured rotational velocities are expected to spin below the critical value before collapse and are thus predicted to vanish without a trace.

Unified Astronomy Thesaurus concepts: Relativistic disks (1388); Accretion (14); Massive stars (732); Hydrodynamical simulations (767); General relativity (641)

1. Introduction

Recent evidence for the disappearance of massive stars (Gerke et al. 2015; Adams et al. 2017; Allan et al. 2020) emphasizes the importance of studying the formation of black holes (BHs) and the conditions under which their formation might trigger a bright transient event (Fryer 1999; Woosley & Heger 2006; Lovegrove & Woosley 2013; Kochanek 2015; Smartt 2015; Sukhbold et al. 2016).

It is widely believed that the lack of a bright transient is due to the collapse of a slowly rotating star (Fryer 1999; Smartt 2015). In this scenario, it is commonly assumed that the central engine involves a newly formed BH accreting material from the collapsing star. The properties of the inflowing material depend on the internal structure of the pre-collapse star and, in particular, its angular momentum (Lee & Ramirez-Ruiz 2006; Zalamea & Beloborodov 2009; Perna et al. 2014). The angular momentum content of the stellar progenitor is a key ingredient, as even a small amount of rotation can break spherical symmetry and could produce a centrifugally supported accretion disk, which will evolve via internal magnetohydrodynamic (MHD) stresses (Balbus & Hawley 1991). It has been noted that even in the absence of rotation, convective motions in the outer parts of highly evolved stars could also produce accretion disks (Gilkis & Soker 2014, 2016; Quataert et al. 2019).

Spherical accretion onto BHs is relatively inefficient at producing feedback because the material is compressed but not shocked, and thus cannot effectively convert gravitational to thermal energy (Bondi 1952; Blondin & Raymer 2012). This changes dramatically when the infalling material has a critical amount of specific angular momentum (Fryxell & Taam 1988; MacLeod & Ramirez-Ruiz 2015). When this is the case and if material is injected at large radii, a standard accretion disk will form. Disk material will then gradually spiral inwards as internal MHD stress transports its angular momentum outward.

Accretion disks naturally produce MHD winds, which carry both bulk kinetic energy and ordered Poynting flux (Tchekhovskoy et al. 2011; McKinney et al. 2012). The energy released by this accretion disk feedback is expected to be significantly larger than the binding energy of the star (Kohri et al. 2005; Yuan & Narayan 2014), which implies that the motion of the inflowing stellar gas can be effectively reversed. If the inflow is halted, we can then set constraints on the final mass and spin of the newly formed BH (Batta & Ramirez-Ruiz 2019). Our understanding of the fate of the collapsing star thus depends on our ability to determine the critical specific angular momentum below which material is able to accrete without generating feedback.

General relativity plays a crucial role and sets the specific angular momentum at the innermost stable circular orbit (ISCO). The flow pattern changes dramatically if the specific angular momentum of the inflowing material is near this critical

value, as gas will not only be compressed but will be able to dissipate its motion perpendicular to the plane of symmetry and form a disk that is only marginally supported by rotation (Beloborodov & Illarionov 2001; Lee & Ramirez-Ruiz 2006; Zalamea & Beloborodov 2009). As the specific angular momentum increases, the rotational support becomes progressively more dominant until a standard Keplerian disk is formed. In this Letter we perform the first multidimensional general relativistic simulations of uniformly rotating, low angular momentum non-magnetized flows (Section 2), in order to derive the properties of the flow near this critical transition (Section 3) and establish when feedback becomes relevant (Section 4). We then make use of these results to obtain an upper limit on the angular momentum that would allow the observed massive stellar progenitors to vanish without a trace (Section 5).

2. Numerical Setup and Initial Conditions

We performed two-dimensional numerical simulations of low angular momentum, flows using the Eulerian code HARM (Gammie et al. 2003; Noble et al. 2006), which solves the equations of general relativistic MHD. Our setup consists of a quasi-radial inflow of non-magnetized gas onto an accreting BH. The infalling gas has specific angular momentum near the critical value, defined as that assigned to the ISCO of a BH. The numerical setup is similar to the one described in Suková & Janiuk (2015), Suková et al. (2017), Janiuk et al. (2018), and Palit et al. (2019).

The boundary conditions in the angular direction are set to be periodic, while the outer inner boundary is set to be outflowing and the outer radial boundary is set to the inflow condition. This boundary is placed at large enough radii such that it will not impact the central region over the duration of the simulation ($\approx$300 r_g/c; Suková et al. 2017).

The units of the code are in the geometric system in which lengths are expressed in terms of the gravitational radius

$$r_\mathrm{g} = \frac{GM_\mathrm{bh}}{c^2}, \qquad (1)$$

where M_bh is the mass of the BH. For converting to cgs units, we used the same convention as that described in Janiuk (2019). In this convention, if $M_\mathrm{bh} = 1\ M_\odot$, the time unit is 5×10^{-6} s and $r_\mathrm{g} = 1.48$ km. In our particular case, we choose $M_\mathrm{bh} = 20\ M_\odot$, which corresponds to a time unit of 9.9×10^{-5} s, and a length unit of 29.5 km. For our simulations, the enclosed mass in the computational domain, defined as $2\pi \int_0^\pi \int_{R_\mathrm{in}}^{R_\mathrm{domain}} \rho \sqrt{-g}\, dr d\theta$, is chosen to be 0.2 $M_\odot$ (where g is the determinant of the metric, R_in is the inner radius, and R_domain is the domain size), which in turn corresponds to a mass accretion rate of 0.1 $M_\odot$ s^{-1}.

The domain covers $R_\mathrm{domain} = 200\ r_\mathrm{g}$ around the BH for simulations with a non-spinning BH, and $R_\mathrm{domain} = 100\ r_\mathrm{g}$ for simulations with spin. The resolution is 800×800 cells in the x_1 and x_2 directions, where x_1 and x_2 are the coordinates in spherical Kerr–Schild form for a non-spinning BH, and 400×400 for a BH with spin. The initial radial component of the velocity (u^r) of the material is determined by the relativistic version of the Bernoulli equation (Shapiro & Teukolsky 1986). In this formalism, the critical point (r_s, where subscript s stands for the sonic point), where the flow becomes supersonic, is set as a free parameter. In this case, the

critical point lies outside the domain at $r_\mathrm{s} = 1000\ r_\mathrm{g}$, resembling a collapsing 34 $M_\odot$ star from models of Woosley & Heger (2006). This implies that matter is always supersonic within our computational domain. The fluid is considered a polytrope with a pressure $P = K\rho^\gamma$, where ρ is the density, $\gamma = 4/3$ is the adiabatic index, and K is the specific entropy, in this case taken to be that of a relativistic fluid with inefficient cooling. In what follows we describe how we generate the initial conditions.

Once the critical point is determined, the velocity at this critical point is (Shapiro & Teukolsky 1986)

$$[u_\mathrm{s}^r]^2 = \frac{GM_\mathrm{bh}}{2r_\mathrm{s}}, \qquad (2)$$

where r is the radial coordinate and u^r is the radial component of the four-velocity. The radial velocity can be obtained by numerically solving the relativistic Bernoulli equation:

$$\left(1 + \frac{\gamma}{\gamma - 1}\frac{P}{\rho}\right)^2 \left(1 - \frac{2GM_\mathrm{bh}}{r} + [u^r]^2\right) = \text{constant}, \qquad (3)$$

and the density is set by the mass accretion rate $\dot{M}$:

$$\rho = \frac{\dot{M}}{4\pi r^2 u^r}. \qquad (4)$$

The specific entropy value, K, depends on the radial velocity and is taken to be (Suková & Janiuk 2015; Suková et al. 2017; Palit et al. 2019)

$$K = \left(u^r 4\pi r^2 \frac{c_\mathrm{s}^{\frac{2}{\gamma-1}}}{\gamma^{\frac{1}{\gamma-1}}\dot{M}}\right)^{\gamma-1}, \qquad (5)$$

where $c_\mathrm{s}^2 = \frac{\gamma P}{\rho}$ is the local sound speed.

In order to derive the angular velocity at each radius, we use the specific energy and angular momentum at the ISCO (Suková & Janiuk 2015; Suková et al. 2017; Palit et al. 2019):

$$\epsilon_\mathrm{isco} = -u_{t,\mathrm{isco}} = \frac{1 - 2/r_\mathrm{isco} + a/r_\mathrm{isco}^{3/2}}{\sqrt{1 - 3/r_\mathrm{isco} + 2a/r_\mathrm{isco}^{3/2}}} \qquad (6)$$

and

$$l_\mathrm{isco} = u_{\phi,\mathrm{isco}} = \frac{r_\mathrm{isco}^{1/2} - 2a/r_\mathrm{isco} + a^2/r_\mathrm{isco}^{3/2}}{\sqrt{1 - 3/r_\mathrm{isco} + 2a/r_\mathrm{isco}^{3/2}}}, \qquad (7)$$

where the radius of the ISCO r_isco in units of r_g if a function of the dimensionless BH spin a. The angular velocity in Boyer–Lindquist coordinates for a Kerr metric can then be constructed as

$$u^\phi = g^{\phi\nu}u_\nu, \qquad (8)$$

where ν is an index used for Einstein summation notation, ν belongs to $\{t, r, \theta, \phi\}$. For geodesic circular motion at the ISCO, the angular velocity is thus

$$u_\mathrm{isco}^\phi = -g^{\phi t}\epsilon_\mathrm{isco} + g^{\phi\phi}l_\mathrm{isco}, \qquad (9)$$

where the components of the Kerr BH metric are $g^{t\phi} = -2ar/(\Sigma\Delta)$ and $g^{\phi\phi} = (\Delta - a^2\sin^2\theta)/(\Sigma\Delta\sin^2\theta)$, with $\Sigma = r^2 + a^2\cos^2\theta$, $\Delta = r^2 - 2r + a^2$, and θ is the angular coordinate.
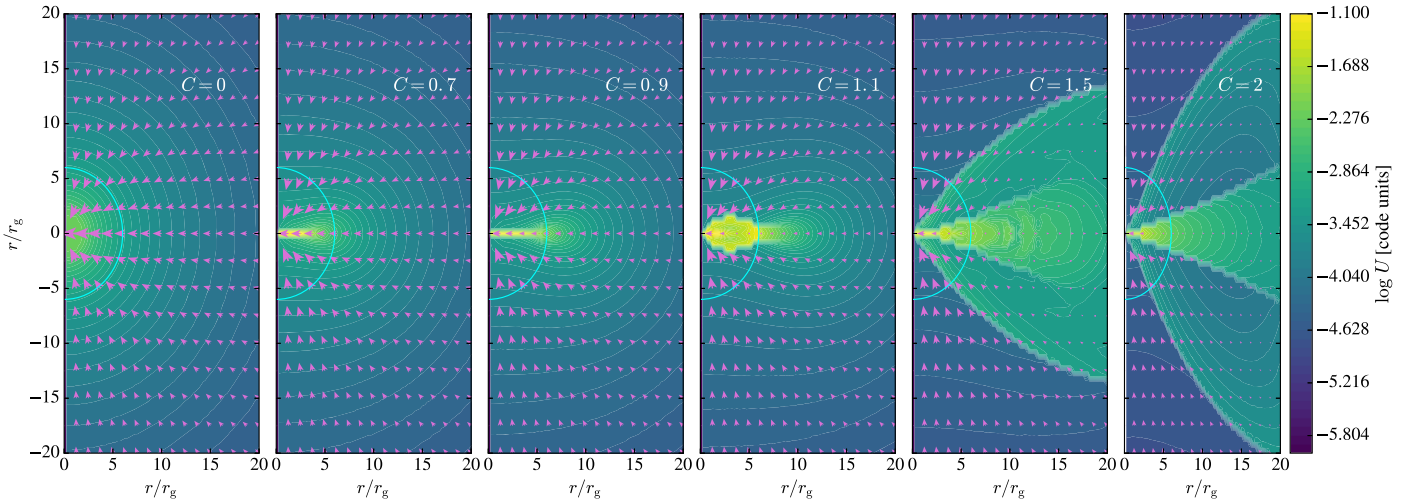
Figure 1. Contour plot of internal energy density (in code units) at $t = 300 r_g/c$ for simulations of initially non-spinning BHs ($a_0 = 0$) with varying C. The arrows represent the velocity vectors of the flow, and the cyan circle shows the location of the ISCO.

In our simulations, we include a factor $C \sin^2 \theta$ in the initial angular velocity profile such that

$$u^\phi = C \sin^2 \theta (-g^{t\phi} \epsilon_{\rm isco} + g^{\phi\phi} l_{\rm isco}). \qquad (10)$$

The factor $\sin^2 \theta$ ensures that the angular momentum vanishes smoothly in the polar regions (Suková et al. 2017), and C is a parameter that we vary. Note that $C = 0$ corresponds to Bondi spherical accretion.

The initial angular momentum per unit mass is then given by $l = u_\phi = g_{\phi\nu} u^\nu$. In the case of $a = 0$, it reduces to

$$l = C l_{\rm isco} \sin^2 \theta. \qquad (11)$$

In what follows we study the outcome of our simulations as we systematically vary C from the classical $C = 0$ (spherical Bondi) to $C = 2$. This allows us to study the formation of accretion disks in low angular momentum flows along with exploring the dissipation of energy in the flow and ensuing feedback.

3. Low Angular Momentum Flows

As the star collapses, material will flow toward the newly formed BH and its angular momentum content will determine the final fate of the accreting object. If there is even a small amount of angular momentum, there will be dissipation of energy at the equator as material is shocked rather than solely compressed (Beloborodov & Illarionov 2001; Lee & Ramirez-Ruiz 2006; Zalamea & Beloborodov 2009).

If the specific angular momentum is below critical, the energy dissipation will be small and the heated gas will be promptly advected onto the BH. This is shown in Figure 1, where we plot contours of internal energy density and velocity vectors from simulations with varying C. The internal energy density in our simulations is related to the pressure as $U = \frac{P}{\gamma - 1}$. As the specific angular momentum increases, material will be marginally bound and shocked near the equator before being accreted. When the angular momentum is near the critical one, a shock discontinuity forms that steadily dissipates energy, which leads to a significant pressure build-up. This is most evidently seen in the simulations at around $C = 1.1$. This pressure build-up slows down the incoming material and produces an angular momentum redistribution

shock. It is noteworthy to point out that this shock is only transonic for the case of $C = 2$. It is useful to compare the energy density in cases with higher angular momentum to the case $C = 0$, where we expect inefficient feedback.

As more material accumulates near the ISCO, the pressure supported structure grows and expands for $C \gtrsim 1.2$, ultimately halting the flow. The top panel of Figure 2 compares the time evolution of the energy dissipation for simulations with $C = 0.9$ and $C = 1.2$. In the case of $C = 0.9$, where the specific angular momentum is below the critical one, the dissipated energy is advected with the flow before being accreted by the BH. When $C = 1.2$ a rotationally supported structure forms, which creates an expanding high-pressure region or *hot bubble*. The energy accumulation in this region continues until the end of the simulations, leading to the steady increase of the bubble's size. This steady accumulation of energy could, in principle, halt the collapse of the infalling star and cause the envelope to be disrupted. The bottom panel of Figure 2 shows the position of the shock in the equatorial plane as a function of time, as well as the velocity of the shock. The shock moves outward with a velocity that is roughly constant in time and is larger than the escape velocity at the outer edge of the computational domain (which is $0.07c$). The material inside the shock will gain internal specific energy similar to the shock's kinetic energy, which is larger than the specific binding energy at the edge of the computational domain. This means that the expanding shock will be able to halt the collapse and effectively unbind the material at the edge of the computational domain. However, this should be treated with caution, because it ignores the pressure from external material, which may act as a lid. In order to reach firm conclusions about the fate of the collapsing star, we need to track the long-term evolution of the shock as it evolves through the entire stellar interior.

We note that in our simulations, we do not include the effects of a changing metric, which are explored by Janiuk et al. (2018). Not surprisingly, the authors found that the BH accretes matter more rapidly for a changing metric, which can potentially alter the critical value of C. However, this effect is only relevant in our simulations at times that are much larger than those currently explored. This is because throughout our simulation, the BH only accretes a fraction $\lesssim 0.01$ of its own mass, and thus the effects of both the self-gravity of the gas
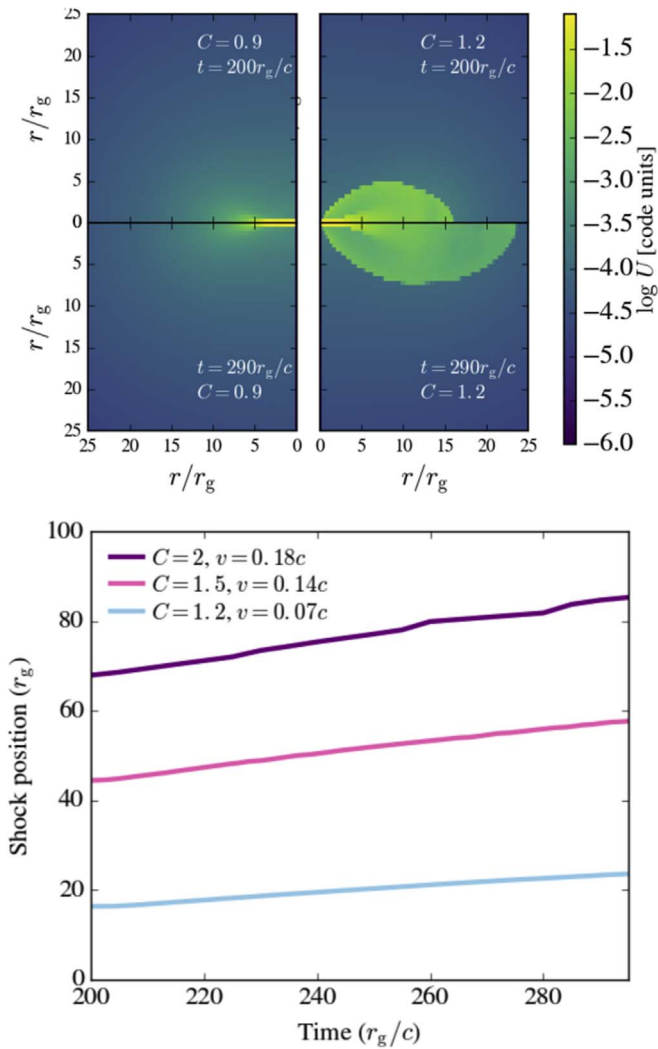
Figure 2. Top panel: the evolution of the internal energy density for two different simulations with $C = 0.9$ and $C = 1.2$ plotted at two different times for BHs with initial spin $a_0 = 0$. The resolution is the same as in Figure 1. Bottom panel: the location of the shock discontinuity in the equatorial plane as a function of time. Plotted here are the shock locations for $C = 2$ (purple line), $C = 1.5$ (pink line), and $C = 1.2$ (blue line). Shown in the legend are the average shock front expansion velocities measured at the equator for the different values of C.

residing in the box and the corresponding change in the metric can be safely ignored. The critical angular momentum can also be altered by the inclusion of magnetic fields in the pre-collapse progenitor as well as the inclusion of radiation feedback. In the former case there can be additional outflows driven by the magnetic field stresses that can inject extra energy into the infalling material (McKinney et al. 2012; Batta & Ramirez-Ruiz 2019; Janiuk 2019). In the latter case, we expect that photons will be entirely advected onto the BH by the very optically thick accretion flow that is many orders of magnitude above the Eddington mass accretion limit in our simulation. The material is also expected to be optically thick to neutrinos, but if hypercritical accretion produces a neutrino-driven outflow, it could further help unbind the star (Kohri et al. 2005).
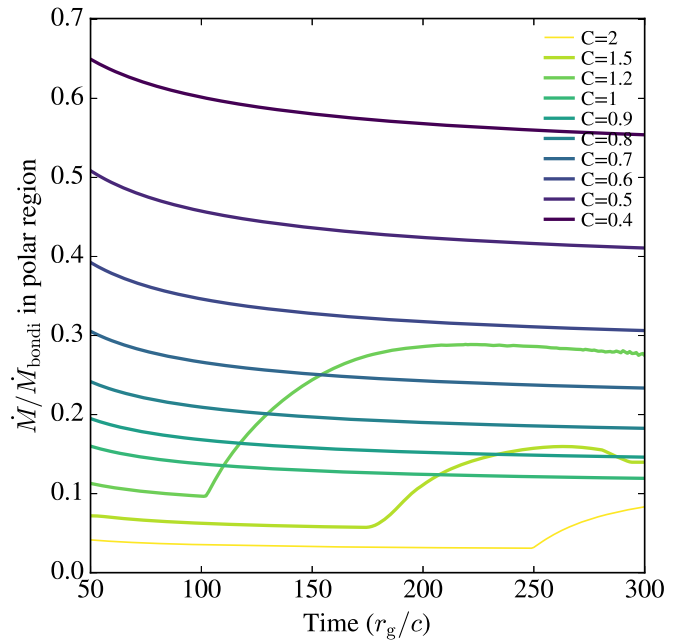

Figure 3. Mass accretion rates (in units of $\dot{M}_{\rm bondi}$) in the polar region for simulations with varying C and initially non-spinning BHs. The values for both $\dot{M}$ and $\dot{M}_{\rm bondi}$ are averaged at the ISCO over one quadrant of the simulation. The polar region is defined here by $0° \leqslant \theta < 60°$, with $\theta = 90$ corresponding to the equatorial plane.

4. Energy Dissipation and Feedback

As shown in Section 3, the dissipation of energy in the infalling gas from a collapsing star with $C \gtrsim 1.2$ can steadily accumulate near the equatorial plane. In this case, the energy dissipation rate exceeds the advection rate as the size of the dissipation region increases and, as a result, a hot pressure region or bubble is produced. This bubble, surrounded by a clear discontinuity in both density and velocity, grows as material continues to be accreted. The corresponding pressure build-up halts the motion of the infalling material in the equatorial plane while increasing the rate of accretion in the polar direction, as material at high latitudes is deflected toward the BH (Figure 1). This can be seen in Figure 3, which shows the accretion rate in the polar direction as a function of time for all simulations with initial $a = 0$ and varying C.

The amount of energy dissipated by accretion is commonly thought to be primarily determined by $\dot{M}$. Yet, because BHs do not have a hard surface, the feedback efficiency cannot be given solely by $\dot{M}$ as in the case of neutron stars or white dwarfs. Nor can BHs build up enough pressure to slow down the infalling gas. Therefore, spherical accretion onto BHs advects any dissipated energy, without appreciable feedback. This situation changes dramatically when the inflow has a non-negligible amount of angular momentum and material is able to form a rotationally supported structure. In these cases, the energy dissipation rate is drastically altered. This can be seen in Figure 4, where we plot in the top panel the internal energy density profile (normalized to Bondi) around the ISCO as a function of θ. In this figure, $\theta = 90°$ corresponds to the equator and $\theta = 0°$ (180°) to the polar direction.

Even though there is internal energy and mass accumulation when $C \lesssim 1.2$, feedback will be inefficient because the flow is supersonic and the internal energy will be advected. The dissipation rate increases dramatically with C as can be seen in
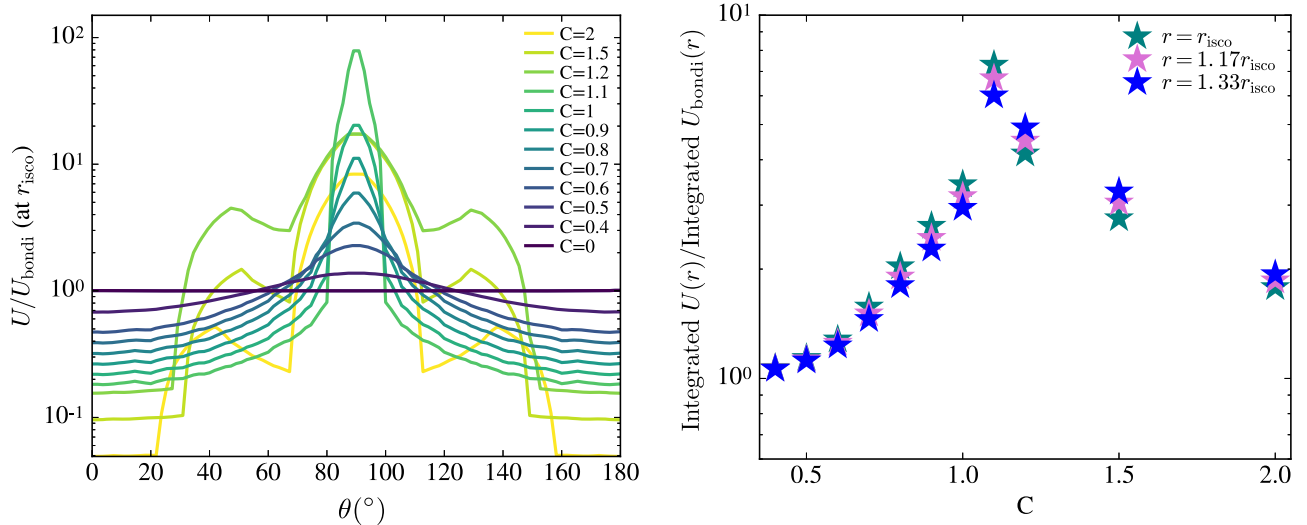
Figure 4. Dissipation of energy in low angular momentum flows. Top panel: internal energy density at the ISCO as a function of θ for initially non-spinning BHs. Here $\theta = 90°$ corresponds to the equator. The normalization factor ($U_{\rm bondi}$) corresponds to $C = 0$ case, which is spherically symmetric accretion and is solely driven by the compression of the flow. Bottom panel: integrated internal energy out to a given radial scale as a function of C. The integrated internal energy is calculated as $U(r) = 2\pi \int_0^\pi \int_{2r_{\rm g}}^r \sqrt{-g(r')}\, U(r')\, dr'\, d\theta$, where g is the determinant of the metric and we use $r = [1, 1.17, 1.33]r_{\rm isco}$. All the analyses make use of the snapshot at $t = 300 r_{\rm g}/c$ for all simulations.

the bottom panel of Figure 4. Plotted in this panel is the integrated energy density out to a given radial coordinate normalized to the classical Bondi case ($C = 0$). The total dissipated energy increases as material with low angular momentum is shocked in the equatorial plane before being advected onto the BH. A noticeable transition occurs at $C \approx 1.2$, as material begins to form a rotationally supported structure. The now differentially rotating flow requires MHD stress in order to dissipate energy and transport angular momentum, thereby enabling the inward accretion of gas. At this stage, the energy dissipation rate decreases as material becomes rotationally supported and shock dissipation is replaced by shear viscosity. In the absence of magnetic fields, shear viscosity in our simulation is driven by numerical dissipation, which also acts over many orbital timescales. We thus caution the reader that the exact value of C from our hydrodynamical simulations might be altered when internal MHD stresses are self-consistently included, as a magnetized outflow can form that can further help halt the stellar collapse (McKinney et al. 2012; Batta & Ramirez-Ruiz 2019; Janiuk 2019). In our current simulations, it is around $C \approx 1.2$ that we see the formation of the hot bubble, which continues to grow as the dissipated energy effectively accumulates near the ISCO (Figure 2). As the angular momentum continues to increase, a disk forms, which halts the advection of material and acts as a feedback term to slow the growth of energy dissipation near the ISCO. We thus conclude that for flows with $C \gtrsim 1.2$, we expect feedback to likely halt the collapse of the infalling star. Because the binding energy of failed supernova progenitors steeply declines with increasing radius, it is suggested that any additional accumulation of energy will ultimately result in the disruption of the entire collapsing progenitor (Batta & Ramirez-Ruiz 2019; Quataert et al. 2019). As the expanding envelope cools and radiation diffuses from it (e.g., Schröder et al. 2020), a transient is expected to accompany the formation of the BH (Fryer 1999; Woosley & Heger 2006; Lovegrove & Woosley 2013;

Kochanek 2015; Smartt 2015; Sukhbold et al. 2016; Quataert et al. 2019).

In addition to the initially non-spinning $a_0 = 0$ BH models, we also ran simulations with $a_0 = 0.05$ and $a_0 = 0.1$ and confirm that the feedback transition also occurs near $C \approx 1.2$ and that the energy dissipation profiles are similar to those plotted in Figure 4. This is consistent with Janiuk et al. (2018), where the authors use a dynamical metric to explore how the accretion onto a BH influences the spin and final mass of the BH. They conclude that different initial spins lead to rather similar qualitative results, as we have found here.

5. Discussion

Having determined the critical specific angular momentum at which accretion onto a BH can generate feedback, we turn our attention to the conditions required for a stellar progenitor to collapse without producing a bright transient under the assumption that significant feedback will unavoidably generate a discernible signal. In what follows, for simplicity, we assume that the star is uniformly rotating.

The corresponding critical angular velocity of the stellar progenitor is quantitatively estimated using the framework established by Batta & Ramirez-Ruiz (2019), in which the formation and evolution of a BH is followed throughout the stellar collapse. For feedback not to be effective, the stellar progenitor needs to satisfy the following condition at all radii:

$$l(r) \leqslant l_{\rm fb}(r) = C_{\rm fb}\, l_{\rm isco}(r). \tag{12}$$

Here $C_{\rm fb}$ is the critical normalization factor taken to be $C_{\rm fb} = 1.2$ and $l_{\rm isco}(r)$ is the specific angular momentum at the ISCO (Bardeen et al. 1972), which evolves as collapsing material is accreted by the BH.

While rotating at such limiting angular velocity, only the star's outermost material has enough specific angular momentum $\Omega_{\rm lim} R_*^2$ to balance the critical condition $C_{\rm fb}\, l_{\rm isco}(R_*)$. At the same time, the rest of the material satisfies condition 12. In the ensuing subsections we express $\Omega_{\rm lim}$ in terms of the star's

break-up angular velocity, $\Omega_{\mathrm{break}} = (GM_*/R_*^3)^{1/2}$, where M_* and R_* are the stellar mass and radius, respectively.

5.1. On the Disappearing Stellar Progenitors of N6946-BH1 and PHL293B-LBV

Let us now turn our attention to the properties of N6946-BH1 and PHL293B-LBV, two stars that have been argued to disappear without an accompanying bright transient (Gerke et al. 2015; Adams et al. 2017; Allan et al. 2020). While other explanations might be viable, a collapse to a BH without feedback is a possible explanation for the sudden disappearance of the star.

We use the stellar evolution code MESA (Paxton et al. 2011, 2013) version 8845 in order to constrain the structure and observational properties of these stars. We use the default MESA parameters for massive stars. For simplicity, our models are non-rotating, and their evolution is halted when carbon burning ends. We ran the models using a Dutch hot wind scheme (Glebbeek et al. 2009) with a scaling factor of 0.8. In this wind scheme, the mass loss rate prescription changes depending on the evolutionary stage of the star. For the rest of this Letter, we take $Z_\odot = 0.02$.

N6946-BH1 is a disappearing star found by Gerke et al. (2015) and Adams et al. (2017) using the Large Binocular Telescope. The star is found to be embedded in a highly dusty environment in the galaxy NGC 6946. This red supergiant star was observed to increase its optical magnitude by around five magnitudes after a weak optical outburst in 2009. One possibility for this disappearing star is a collapse to a BH where the angular momentum was low enough that feedback from the BH was unable to unbind the collapsing progenitor.

Information on the progenitor was deduced using archival data from the Hubble Space Telescope, which was taken around two years before the weak outburst. Using dust and stellar evolution models, Gerke et al. (2015) and Adams et al. (2017) deduced a luminosity of $\log L/L_\odot = 5.29^{+0.04}_{-0.06}$ and a temperature of $T = 3260^{+1670}_{-320}$ K for the pre-collapse progenitor. Their solar-metallicity models constrained the progenitor mass to be $20-30 M_\odot$.

PHL293B-LBV (Allan et al. 2020) is another disappearing star. This luminous blue variable (LBV) was found in the galaxy PHL293B. Allan et al. (2020) used the European Southern Observatory/Very Large Telescope (ESO/VLT)'s ESPRESSO and X-shooter to obtain spectra of this galaxy in 2019. These spectra lacked an LBV signature, which was clearly present from 2011 to 2019. One of many viable possibilities is that when the eruptive period ended, the LBV collapsed into a BH. Using radiative transfer models, Allan et al. (2020) derived a luminosity between $\log L/L_\odot = 6.3-6.7$ and a temperature between $T = 9500 -15,000$ K for the pre-collapse star.

We compare the temperature and luminosity constraints of N6946-BH1 and PHL293B-LBV with our stellar models in order to constrain both their masses and internal structures. The left panel of Figure 5 shows the locations of N6946-BH1 and PHL293B-LBV on the Hertzsprung–Russell (HR) diagram together with the MESA stellar evolutionary models. The solid lines correspond to models with $Z = Z_\odot$, which are relevant to N6946-BH1 (Gerke et al. 2015; Adams et al. 2017), while the dotted lines correspond to models with $Z = 0.02Z_\odot$, appropriate for PHL293B-LBV (Allan et al. 2020). Using these models we constrain the initial masses of N6946-BH1 and

PHL293B-LBV to be $23-28\ M_\odot$ and $98-130\ M_\odot$, respectively. These constraints are consistent with those quoted in the literature. We caution the reader that given the mass range deduced for PHL293B-LBV, the final outcome could be a pair instability supernova (Woosley 2017). Nonetheless, the lack of a transient event for PHL293B-LBV suggests that this was not the case, as argued by Allan et al. (2020).

We use these models to also constrain the internal density structure of the progenitor, which in turn sets the moment of inertia and allows us to place a limit on the maximum angular velocity needed for the star to collapse without forming a disk. These limits for N6946-BH1 and PHL293B-LBV are plotted in the middle panel of Figure 5. Within the hatched region, the angular velocity of the pre-collapse progenitor is below the critical one in which feedback becomes efficient. The regions extends to higher fractions of the break-up velocity for high-mass solar-metallicity stars because these stars self-strip due to rapid wind-driven mass loss, leaving behind compact, low moment of inertia Wolf–Rayet stars. We thus suggest that progenitors within this region will collapse without producing a bright transient.

5.2. Is it Common for Stars to Vanish without a Trace?

In the preceding sections we have endeavored to outline the rotational constraints needed for stellar progenitors to vanish without a trace. We caution that even in the absence of rotation, the outer layers might be still ejected by, for example, the loss of rest mass energy via neutrinos (e.g., Lovegrove & Woosley 2013) and could still produce a faint transient signal (e.g., MacLeod et al. 2017).

Herein we assume that stellar spin is an essential parameter and turn to the problem of assembling the pre-collapse rotational constraints derived in this Letter into a general scheme involving the evolution of massive stars. In the right panel of Figure 5 we plot the observationally derived rotation rates of single O-type ($Z = 0.2\ Z_\odot$) stars taken from Ramírez-Agudelo et al. (2013) with initial stellar masses derived by Weidner & Vink (2010).

We produce MESA models to match the age and stellar mass of these stars, using $Z = 0.2\ Z_\odot$ and assuming rigid-body rotation. Applying the observationally derived rotation rates, we then make use of the following standard relation (Villata 1992):

$$\frac{1}{\Omega}\frac{d\Omega}{dt} = -\frac{1}{I_*}\frac{dI_*}{dt} + \frac{2}{3}\frac{R_*^2}{I_*}\frac{dM_*}{dt}. \qquad (13)$$

Where M_* and R_* are the stellar mass and radius, respectively, $I_* = \frac{8\pi}{3}\int_0^{R_*}\rho(r)r^4 dr$ is the moment of inertia of the star, and Ω is the angular velocity. The evolution of the rotational velocity is then computed until the end of the star's life, which in our models corresponds to the end of carbon burning. In the right panel of Figure 5 we plot the final rotational velocity derived for each observed system with the corresponding symbols labeled as *Evolved data*.

Throughout this Letter, we have assumed rigid-body rotation, i.e., very efficient angular momentum transport within the star. It is evident that the mechanisms responsible for transporting angular momentum inside massive stars are not well understood currently (Kissin & Thompson 2015; Fuller & Ma 2019). Even in the simplest case of uniform rotation, we find that stellar winds can extract a significant amount of
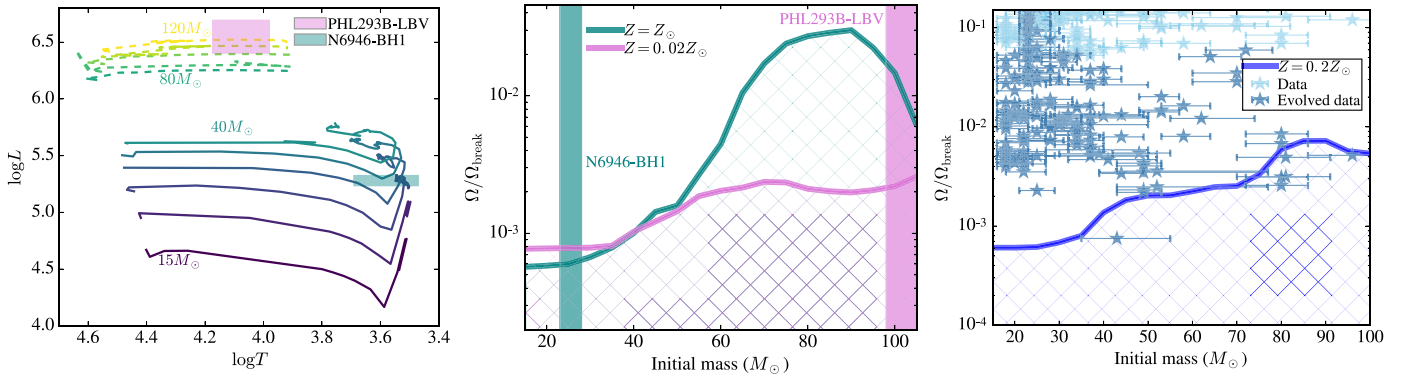
Figure 5. Left panel: Hertzsprung–Russell (HR) diagram of the MESA models used in our analysis (Paxton et al. 2011, 2013). The solid lines are models with $Z = Z_\odot$. The solid lines are stellar models that start at $M_{ZAMS} = 15\ M_\odot$ and are plotted every 5 $M_\odot$ until 40 $M_\odot$. In teal we show the luminosity and temperature constraints for N6946-BH1 (Gerke et al. 2015; Adams et al. 2017). The dotted lines represent models with $Z = 0.02\ Z_\odot$. Models start at $M_{ZAMS} = 80\ M_\odot$ and are plotted every 10 $M_\odot$ until 120 $M_\odot$. Models with $Z = 0.02\ Z_\odot$ were used to constrain PHL293B-LBV (Allan et al. 2020), whose luminosity and temperature constraints are shown in orchid. Middle panel: maximum angular velocity at which a star can disappear without an accompanying bright transient as a function of the initial mass of the progenitor. Here Ω_{break} is the break-up velocity. The different lines are the constraints derived at different metallicities, which have been selected to match those of N6946-BH1 and PHL293B-LBV. Also plotted are the mass estimates we derive from our MESA models. Models in this specific mass range spend a fraction of their last 10^4 yr of evolution within the corresponding uncertainty region in the HR diagram (left panel). Right panel: angular velocity as a function of the initial mass of the stellar progenitor. Plotted are the rotational velocities of single O-type stars at $Z = 0.2 Z_\odot$ taken from Ramírez-Agudelo et al. (2013), with masses derived by Weidner & Vink (2010). We evolve the rotational velocities of MESA models of these O-type stars by applying Equation (13) and assuming rigid-body rotation until carbon burning ends (see the text for details about this assumption). These pre-collapse rotational velocities, labeled as *evolved data*, are compared with the range of angular velocities for these stars to collapse without an accompanying bright transient (*hatched* region).

angular momentum from the star and in a small fraction of cases produce rotation rates close to those required for stars to vanish without a trace (right panel of Figure 5). More specifically, we find that $\approx 5\%$ of the stars we evolved (from a total of 163) have (Ω/Ω_{break}) below the critical value (hatched region in the right panel of Figure 5). In these cases we expect the collapse to proceed without the formation of an accretion disk, allowing the progenitor to vanish in our model.

Although the evolution of O-type stars may be be commonly associated with supernovae, some of them might be expected to disappear. If single O-type stars with (Ω/Ω_{break}) below the critical value are expected to vanish, we then conclude that these objects are at least tens of times rarer than standard supernova events. This of course has been derived under the assumption that a standard supernova event is the natural outcome for the vast majority of O-type stars with (Ω/Ω_{break}) above the critical value. Obviously, the above calculation is limited and should be taken as an order of magnitude estimate at present. For example, using the same Dutch hot wind scheme in MESA but with a scaling factor of 1.0 (instead of the standard 0.8) we find that $\approx 7\%$ of the stars we evolved have (Ω/Ω_{break}) below the critical (mass-dependent) value.

This simple estimate for the rate of disappearing massive stars should improve as more objects have their rotational rates measured and massive stellar evolution modeling improves. Having said this, it is important to note that this few percent estimate is roughly consistent with the one derived by Gerke et al. (2015), where they argued that the current rate of vanishing stars is $\gtrsim 7\%$ the rate of core-collapse supernova. This estimate can also be altered for red supergiants, as convective motions in their outer layers might produce accretion disks and thus effective feedback even in the absence of net rotation (Quataert et al. 2019).

Most massive stars are born in binaries, and binary interactions can significantly impact stellar structure and stellar rotation through mass transfer and tides (Sana et al. 2012).

Accounting for the impact of binary evolution would further change the expected fraction of vanishing stars.

Many core collapses of massive stars are expected to produce supernovae when forming neutron stars in spherical explosions (Ugliano et al. 2012; Sukhbold et al. 2016) but some are expected to have insufficient neutrino deposition (Woosley 1993; Fryer et al. 2009; Lazzati et al. 2012; Lovegrove & Woosley 2013) and will form a BH in the center of the star.

The modeling of stellar collapse leading to BH formation is a formidable challenge to computational techniques. It is also a formidable challenge for observers, in their quest for finding stars that disappear. If we were to venture on a general classification scheme for failed supernovae, on the hypothesis that the central object involves a BH formed in a core-collapse explosion, we expect the specific angular momentum of the infalling stellar material to be a critical parameter. When $l(r) \lesssim l_{fb}(r)$ we predict the star will vanish without a trace. On the other hand, when $l(r) \gtrsim l_{fb}(r)$ the collapse may instead be followed by a bright transient, whose properties will likely depend on the mass and spin of the BH, the rate at which gas is supplied, the spin orientation relative to our line of sight, and the structure of the envelope through which any outflows will be re-processed.

ORCID iDs

Ariadna Murguia-Berthier ⓘ https://orcid.org/0000-0003-2333-6116
Aldo Batta ⓘ https://orcid.org/0000-0002-3269-3847
Agnieszka Janiuk ⓘ https://orcid.org/0000-0002-1622-3036
Enrico Ramirez-Ruiz ⓘ https://orcid.org/0000-0003-2558-3102
Ilya Mandel ⓘ https://orcid.org/0000-0002-6134-8946
Scott C. Noble ⓘ https://orcid.org/0000-0003-3547-8306
Rosa Wallace Everson ⓘ https://orcid.org/0000-0001-5256-3620

References

Adams, S. M., Kochanek, C. S., Gerke, J. R., Stanek, K. Z., & Dai, X. 2017, MNRAS, 468, 4968
Allan, A., Groh, J., Mehner, A., et al. 2020, MNRAS, 496, 1902
Balbus, S. A., & Hawley, J. F. 1991, ApJ, 376, 214
Bardeen, J. M., Press, W. H., & Teukolsky, S. A. 1972, ApJ, 178, 347
Batta, A., & Ramirez-Ruiz, E. 2019, arXiv:1904.04835
Beloborodov, A. M., & Illarionov, A. F. 2001, MNRAS, 323, 167
Blondin, J. M., & Raymer, E. 2012, ApJ, 752, 30
Bondi, H. 1952, MNRAS, 112, 195
Fryer, C. L. 1999, ApJ, 522, 413
Fryer, C. L., Brown, P. J., Bufano, F., et al. 2009, ApJ, 707, 193
Fryxell, B. A., & Taam, R. E. 1988, ApJ, 335, 862
Fuller, J., & Ma, L. 2019, ApJL, 881, L1
Gammie, C. F., McKinney, J. C., & Tóth, G. 2003, ApJ, 589, 444
Gerke, J. R., Kochanek, C. S., & Stanek, K. Z. 2015, MNRAS, 450, 3289
Gilkis, A., & Soker, N. 2014, MNRAS, 439, 4011
Gilkis, A., & Soker, N. 2016, ApJ, 827, 40
Glebbeek, E., Gaburov, E., de Mink, S. E., Pols, O. R., & Portegies Zwart, S. F. 2009, A&A, 497, 255
Janiuk, A. 2019, ApJ, 882, 163
Janiuk, A., Sukova, P., & Palit, I. 2018, ApJ, 868, 68
Kissin, Y., & Thompson, C. 2015, ApJ, 808, 35
Kochanek, C. S. 2015, MNRAS, 446, 1213
Kohri, K., Narayan, R., & Piran, T. 2005, ApJ, 629, 341
Lazzati, D., Morsony, B. J., Blackwell, C. H., & Begelman, M. C. 2012, ApJ, 750, 68
Lee, W. H., & Ramirez-Ruiz, E. 2006, ApJ, 641, 961
Lovegrove, E., & Woosley, S. E. 2013, ApJ, 769, 109
MacLeod, M., Macias, P., Ramirez-Ruiz, E., et al. 2017, ApJ, 835, 282
MacLeod, M., & Ramirez-Ruiz, E. 2015, ApJ, 803, 41
McKinney, J. C., Tchekhovskoy, A., & Bland ford, R. D. 2012, MNRAS, 423, 3083
Noble, S. C., Gammie, C. F., McKinney, J. C., & Del Zanna, L. 2006, ApJ, 641, 626
Palit, I., Janiuk, A., & Sukova, P. 2019, MNRAS, 487, 755
Paxton, B., Bildsten, L., Dotter, A., et al. 2011, ApJS, 192, 3
Paxton, B., Cantiello, M., Arras, P., et al. 2013, ApJS, 208, 4
Perna, R., Duffell, P., Cantiello, M., & MacFadyen, A. I. 2014, ApJ, 781, 119
Quataert, E., Lecoanet, D., & Coughlin, E. R. 2019, MNRAS, 485, L83
Ramírez-Agudelo, O. H., Simón-Díaz, S., Sana, H., et al. 2013, A&A, 560, A29
Sana, H., de Mink, S. E., de Koter, A., et al. 2012, Sci, 337, 444
Schrøder, S. L., MacLeod, M., Loeb, A., Vigna-Gómez, A., & Mandel, I. 2020, ApJ, 892, 13
Shapiro, S. L., & Teukolsky, S. A. 1986, Black Holes, White Dwarfs and Neutron Stars: The Physics of Compact Objects (New York: Wiley)
Smartt, S. J. 2015, PASA, 32, e016
Sukhbold, T., Ertl, T., Woosley, S. E., Brown, J. M., & Janka, H. T. 2016, ApJ, 821, 38
Suková, P., Charzyński, S., & Janiuk, A. 2017, MNRAS, 472, 4327
Suková, P., & Janiuk, A. 2015, MNRAS, 447, 1565
Tchekhovskoy, A., Narayan, R., & McKinney, J. C. 2011, MNRAS, 418, L79
Ugliano, M., Janka, H., Arcones, A., & Marek, A. 2012, in ASP Conf. Ser. 453, Explosion and Remnant Systematics of Neutrino-driven Supernovae for Spherically Symmetric Models, ed. R. Capuzzo-Dolcetta, M. Limongi, & A. Tornambè (San Francisco, CA: ASP), 91
Villata, M. 1992, MNRAS, 257, 450
Weidner, C., & Vink, J. S. 2010, A&A, 524, A98
Woosley, S. E. 1993, ApJ, 405, 273
Woosley, S. E. 2017, ApJ, 836, 244
Woosley, S. E., & Heger, A. 2006, ApJ, 637, 914
Yuan, F., & Narayan, R. 2014, ARA&A, 52, 529
Zalamea, I., & Beloborodov, A. M. 2009, MNRAS, 398, 2005